JOURNAL OF SPACECRAFT AND ROCKETS
Vol. 32, No. 5, September–October 1995

Wake Flow About the Mars Pathfinder Entry Vehicle

R. A. Mitcheltree* and P. A. Gnoffo†
NASA Langley Research Center, Hampton, Virginia 23681-0001

A computational approach is used to describe the aerothermodynamics of the Mars Pathfinder vehicle entering the Mars atmosphere at the maximum heating and maximum deceleration points in its trajectory. Ablating and nonablating boundary conditions are developed which produce maximum recombination of CO_2 on the surface. For the maximum heating trajectory point, an axisymmetric, nonablating calculation predicts a stagnation-point value for the convective heating of 115 W/cm^2. Radiative heating estimates predict an additional 5–12 W/cm^2 at the stagnation point. Peak convective heating on the afterbody occurs on the vehicle's flat stern with a value of 5.9% of the stagnation value. The forebody flow exhibits chemical nonequilibrium behavior, and the flow is frozen in the near wake. Including ablation injection on the forebody lowers the stagnation-point convective heating 18%.

Nomenclature

c_i	= mass fraction of species i
D_i	= effective diffusion coefficient for species i, m^2/s
I_i	= molar rate at which species i impacts surface, kg-mole/m$^2 \cdot$ s
J_i	= mass flux of species i due to diffusion, kg/m$^2 \cdot$ s
k_r	= surface reaction rate for reaction r, m/s
M_i	= species molecular weight, kg/kg-mole
$\dot{m}_a$	= ablation blowing rate, kg/m$^2 \cdot$ s
P	= pressure, N/m^2
q_w	= convective heating at wall, W/cm^2
R	= universal gas constant, 8314.3 J/kg-mole $\cdot$ K
$R_{N,\mathrm{eff}}$	= vehicle's effective nose radius, m
s	= distance along body surface, m
T_w	= wall temperature, K
V_∞	= freestream velocity, m/s
x, z	= spatial coordinates, m
y_i	= mole fraction of species i
γ_r	= participation fraction of gaseous reactant
ϵ	= surface emissivity
η	= spatial coordinate normal to wall, m
ρ_i	= density of species i, kg/m^3
σ	= Stefan–Boltzmann constant

Introduction

THE Mars Pathfinder Project[1,2] proposes to land an unmanned probe on Mars to observe the planet's surface and atmosphere. The project focuses on entry, descent, and landing as critical technical challenges. To design the thermal protection system (TPS) for the entry vehicle, an accurate description of the aerothermal environment about the forebody and afterbody is necessary.

Several recent studies[3–10] have predicted the aerothermodynamics on forebodies of vehicles entering the Mars atmosphere. References 3–5 address the Pathfinder mission directly. If the science payload is to be efficiently protected, however, the aerothermodynamics of the afterbody, or near-wake region, must also be described.

Computational methods can be used for this task. The thermochemical nonequilibrium Navier–Stokes tool described in Ref. 3 is used in the present work. It is an application of the LAURA (Langley aerothermodynamic upwind relaxation algorithm) of Gnoffo[11,12] to Mars atmosphere (assumed 97% CO_2 and 3% N_2). For the present study, the code has been further modified to perform an energy balance at the surface and include a fully catalytic CO_2 recombination wall boundary condition with and without ablation-product injection.

Wake flowfields of aeroshell-capped vehicles in air have been examined by numerous authors. Gnoffo has performed such a study with LAURA on lunar return and Mars return vehicles entering Earth's atmosphere.[13] In addition, LAURA solutions have compared well with heating levels measured on the Shuttle Orbiter leeside.[14]

The objective of the present study is to examine the aerothermodynamics about the vehicle entering the Mars atmosphere at the maximum heating point and the maximum deceleration point in its trajectory. Using results from a material response code for ablator response, a full flowfield solution with ablating boundary conditions is also computed for the maximum heating point. Particular attention is given to estimating afterbody heating and describing the near-wake flow.

Flowfield Computational Tool

LAURA is an upwind-biased, point-implicit relaxation algorithm[12] for obtaining the numerical solution to the governing equations for three-dimensional, viscous, hypersonic flows in thermochemical nonequilibrium. The algorithm is based on a finite-volume formulation in which the inviscid fluxes are described by Roe's averaging with second-order corrections based on Yee's symmetric total-variation-diminishing scheme. The governing equations include continuity equations for 14 species, three momentum equations (one of which is extraneous for the axisymmetric cases), and two energy equations describing the conservation of vibrational–electronic and total energies. For the present Mars atmosphere study, the 14 species are CO_2, CO, N_2, O_2, NO, C, N, O, SiO, H_2, C_2, C_3, H, and Si. (The last six species maintain trace concentrations except in the solution with ablation.) A 24-reaction chemical-kinetics model is used. The reactions and rates are tabulated in Ref. 15. No appreciable degree of ionization is expected at these conditions. All transport properties for the species come from collision integrals, which are computed from Lennard–Jones potentials. Description of the transport properties and details on the remainder of the physical models are included in Refs. 3 and 11.

Computational simulations of Mars entries suffer many limitations. The flowfield is assumed to be steady and laminar. Unsteady effects are small at these high speeds, but transition to turbulence could occur, particularly at the maximum-deceleration trajectory point. Unfortunately, no available turbulence models have been shown to be valid in the wake regions of blunt bodies. In addition, many of the physical models used in the calculation are derived from

---

Presented as Paper 94-1958 at the AIAA/ASME Joint Thermophysics and Heat Transfer Conference, Colorado Springs, CO, June 20–23, 1994; received Aug. 15, 1994; revision received Jan. 10, 1995; accepted for publication May 29, 1995.

*Aerospace Engineer, Aerothermodynamics Branch, Gas Dynamics Division. Senior Member AIAA.

†Senior Research Engineer, Aerothermodynamics Branch, Gas Dynamics Division. Associate Fellow AIAA.

experimental data from compressive flows. Their applicability in the expanding regions of these flows is uncertain. Two additional limitations of the present method can produce elemental separation in the boundary layer. First, the multicomponent averaging procedure used to define the diffusion coefficients does not force the mass flux due to diffusion to sum to zero. Second, implementation of the flux limiters in the boundary layer may result in different difference stencils being used on different equations. Finally, transport properties may not be accurate at temperatures above 10,000 K or below 1000 K.

Results presented are computed on a Cray C-90. An axisymmetric solution requires 3 to 6 h of computational time.

Surface Boundary Conditions

Species Continuity Equations

In the present work, both ablating and nonablating boundary conditions are examined. In each case, since the degree of wall catalysis in CO_2 is unknown, the wall's effect on the flow is assumed to cause maximum recombination of CO_2. Maximum recombination of CO_2 should produce an upper-bound prediction for the convective heating, and for this study, no other wall recombination is considered.

Recombination of a dissociated gas mixture on a solid involves numerous complex phenomena. The present approximation estimates the upper limit of recombination by recognizing that such a process is limited by three rates: the rate by which reactants diffuse toward the wall, the frequency at which the reactants strike the wall, and the rate at which products can diffuse from the wall. Comment on the boundary condition's extension to the ablating case is included at the end of the section.

Assuming that the Rideal–Eley mechanism[16] is the only reaction mechanism, CO_2 surface recombination can be written as four first-order reactions:

$$O + [_s] \rightarrow O_s \tag{1}$$

$$CO + O_s \rightarrow CO_2 + [_s] \tag{2}$$

$$CO + [_s] \rightarrow CO_s \tag{3}$$

$$O + CO_s \rightarrow CO_2 + [_s] \tag{4}$$

where the subscript s refers to the surface-adsorbed reactant and $[_s]$ is an available adsorption site on the surface.

The mass flux due to the reactions, J_i, must be balanced by diffusion. Using the same quasi-binary-diffusion approximation to multicomponent diffusion used in LAURA,[11] we have

$$J_O = -k_1\rho_O - k_4\rho_O = -\rho D_O \frac{\partial y_O}{\partial \eta} \tag{5}$$

$$J_{CO} = -k_2\rho_{CO} - k_3\rho_{CO} = -\rho D_{CO} \frac{\partial y_{CO}}{\partial \eta} \tag{6}$$

$$J_{CO_2} = k_2\rho_{CO}\frac{M_{CO_2}}{M_{CO}} + k_4\rho_O\frac{M_{CO_2}}{M_O} = -\rho D_{CO_2}\frac{\partial y_{CO_2}}{\partial \eta} \tag{7}$$

This approximation to multicomponent diffusion can be formulated in terms of the mass-fraction or mole-fraction gradient. The definition of the effective binary-diffusion coefficients is dependent on this choice. In the present work, as in LAURA, mole-fraction gradients are used, following the method of Lee.[17]

The reactions rates are

$$k_1 = \gamma_1\sqrt{\frac{RT_w}{2\pi M_O}} \tag{8}$$

$$k_2 = \gamma_2\sqrt{\frac{RT_w}{2\pi M_{CO}}} \tag{9}$$

$$k_3 = \gamma_3\sqrt{\frac{RT_w}{2\pi M_{CO}}} \tag{10}$$

$$k_4 = \gamma_4\sqrt{\frac{RT_w}{2\pi M_O}} \tag{11}$$

where γ_r is the fraction of gaseous-reactant particles striking the wall that participate in the reaction. For example, γ_1 is the fraction of O atoms striking the surface that are adsorbed. To obtain a boundary condition from Eqs. (5–11) requires additional equations relating the γ_r.

Conservation of mass in a steady flow requires the surface coverage of O_s and CO_s to remain constant; thus,

$$\gamma_1 = \gamma_2\frac{c_{CO,w}}{c_{O,w}}\left(\frac{M_O}{M_{CO}}\right)^{\frac{3}{2}} \tag{12}$$

$$\gamma_4 = \gamma_3\frac{c_{CO,w}}{c_{O,w}}\left(\frac{M_O}{M_{CO}}\right)^{\frac{3}{2}} \tag{13}$$

where $c_{i,w}$ is the mass fraction of species i at the wall. With these relations, $J_O + J_{CO} + J_{CO_2} = 0$ in Eqs. (5–7). Equations (12) and (13), along with the restriction that $0 \le \gamma_r \le 1$, $\gamma_1 + \gamma_4 \le 1$, and $\gamma_2 + \gamma_3 \le 1$, establish the boundary condition. In particular, if

$$c_{O,w} \le c_{CO,w}\left(\frac{M_O}{M_{CO}}\right)^{\frac{3}{2}} \tag{14}$$

maximum CO_2 recombination is caused by setting

$$\gamma_1 + \gamma_4 = 1 \tag{15}$$

$$\gamma_2 = \gamma_1\frac{c_{O,w}}{c_{CO,w}}\left(\frac{M_{CO}}{M_O}\right)^{\frac{3}{2}} \tag{16}$$

and

$$\gamma_3 = \gamma_4\frac{c_{O,w}}{c_{CO,w}}\left(\frac{M_{CO}}{M_O}\right)^{\frac{3}{2}} \tag{17}$$

Conversely, if

$$c_{CO,w} < c_{O,w}\left(\frac{M_{CO}}{M_O}\right)^{\frac{3}{2}} \tag{18}$$

maximum CO_2 recombination is caused by setting

$$\gamma_2 + \gamma_3 = 1 \tag{19}$$

and using Eqs. (12) and (13) for γ_1 and γ_4.

A physical interpretation of these two cases can be extracted. From kinetic theory, the molar rate at which a gaseous species impacts the surface, I_i, is the product of its local concentration with its thermal velocity divided by 4. For O, the expression is

$$I_O = \frac{\rho_{O,w}}{M_O}\sqrt{\frac{RT_w}{2\pi M_O}} \tag{20}$$

For CO, the expression is

$$I_{CO} = \frac{\rho_{CO,w}}{M_{CO}}\sqrt{\frac{RT_w}{2\pi M_{CO}}} \tag{21}$$

If $I_O < I_{CO}$, then the inequality of (14) holds and the maximum recombination of CO_2 is limited by the availability of O. In particular, the recombination in the reaction (2) cannot proceed faster than the maximum rate at which the reaction (1) can supply adsorbed O. In addition, since the CO_s surface coverage is constant, CO cannot be adsorbed in the reaction (3) faster than the reaction (4) removes CO_s.

For the second case, when $I_{CO} < I_O$, the inequality (18) holds and the maximum recombination of CO_2 is limited by the availability of CO.

Expressions for species mass fractions at the wall can be written from Eqs. (5–7):

$$c_{\mathrm{O},w} = \frac{c_{\mathrm{O},w+1} M_{m,w+1}}{M_{m,w} + (k_1 + k_4)(\Delta\eta\, M_{\mathrm{O}}/D_{\mathrm{O}})} \tag{22}$$

$$c_{\mathrm{CO},w} = \frac{c_{\mathrm{CO},w+1} M_{m,w+1}}{M_{m,w} + (k_2 + k_3)(\Delta\eta\, M_{\mathrm{CO}}/D_{\mathrm{CO}})} \tag{23}$$

$$c_{\mathrm{CO_2},w} = c_{\mathrm{CO_2},w+1}\frac{M_{m,w+1}}{M_{m,w}} + \frac{\Delta\eta\, M_{\mathrm{CO_2}}}{D_{\mathrm{CO_2}} M_{m,w}}\left(k_2 c_{\mathrm{CO},w}\frac{M_{\mathrm{CO_2}}}{M_{\mathrm{CO}}} + k_4 c_{\mathrm{O},w}\frac{M_{\mathrm{CO_2}}}{M_{\mathrm{O}}}\right) \tag{24}$$

The subscript $w + 1$ refers to the location $\Delta\eta$ above the wall. The wall temperature required in evaluating $k_1 - k_4$ is the radiative equilibrium value discussed below. The molecular weight of the mixture at the wall is obtained from the definition of molecular weight:

$$M_{m,w} = \frac{1}{\sum c_{i,w}/M_i} \tag{25}$$

where the mass fractions for the remainder of the species are obtained from a noncatalytic wall boundary condition

$$c_{i,w} = c_{i,w+1} \tag{26}$$

To preserve the simple explicit formulation for the mass fractions of Eqs. (22–24) in the numerical implementation, the value for the wall-mixture molecular weight is computed from the previous iteration's wall mass fractions.

Combining Eqs. (15–17) with Eqs. (22–24) yields equations for the CO, O, and CO_2 mass fractions at the wall when $I_{\mathrm{O}} < I_{\mathrm{CO}}$. Alternatively, when $I_{\mathrm{CO}} < I_{\mathrm{O}}$, Eqs. (12), (13), and (19) combined with Eqs. (22–24) provide the expressions for the wall mass fractions.

When ablation injection is included, the blowing rate $\dot{m}_a$ and pyrolysis gas composition $c_{i,s}$ from a material response analysis appear in Eqs. (5–7) as

$$\rho D_i \frac{\partial y_i}{\partial \eta} = \dot{m}_a (c_{i,w} - c_{i,s}) - J_i \tag{27}$$

Energy Equations

Boundary conditions for the two energy equations require specification of translational and vibrational–electronic temperatures at the wall. If the assumption of local thermal equilibrium is made at the wall, the two temperatures are equal. For the nonablating boundary condition, an energy balance at the surface sets the temperatures to the radiative equilibrium wall temperature. If q_w is the convective heating at a location on the surface, then the wall temperature T_w is obtained from

$$q_w = \sigma \epsilon T_w^4 \tag{28}$$

where σ is the Stefan–Boltzmann constant. The surface emissivity ϵ of SLA-561 char is assumed to be 0.78 on the forebody and 0.58 on the afterbody. For the ablating boundary condition, the forebody wall temperature is fixed at the value predicted by the material-response analysis.

Ablation Solution

One solution is included with ablation injection defined by a coupled material-response analysis of the forebody.[18] The flowfield code employed in that coupled study used the same chemical kinetics, transport properties, and boundary conditions as those used in the present work. The material-response code was the CMA code[19] working on the ablator material SLA-561. In the present study, the blowing rate, composition, and wall temperature from the material-response analysis at the maximum-heating point in the trajectory are held fixed in the boundary conditions, and the full vehicle flowfield is then computed.

Geometry and Computational Grid

A Viking-style geometry is proposed for the Mars Pathfinder entry vehicle. The forebody is a 70-deg sphere cone with nose radius of 0.6625 m and an overall vehicle diameter of 2.65 m. A 0.06625-m-radius shoulder connects the forebody to a 49.7-deg cone afterbody. (Note: A longer vehicle is now being used for the Mars Pathfinder, whose afterbody cone is 47.44 deg. This slightly longer geometry is not examined in the present paper.)

Creating a grid about the entire entry vehicle is a challenging problem. The hyperbolic grid generator HYPGEN[20] with HGUI (HYPGEN Graphical User Interface) is used to create the single-block grid.

To assure accurate heating predictions, the grid is everywhere orthogonal to the body at its surface. The height of the first cell off the wall is 1.0×10^{-5} m, which yields a cell Reynolds number of 3 based on the local speed of sound at the stagnation point. The grid extends 7.5 vehicle radii downstream. Surface grid distributions are generated using the GRIDGEN[21,22] software. Outer boundary limits are computed from previous elliptically generated grids. The orthogonality is controlled by HYPGEN in combination with three dissipative parameters.

Results

Based on a ballistic coefficient of 55 kg/m^2 and a 7.65-km/s ballistic entry at -14.2 deg, one possible pathfinder trajectory is predicted to encounter maximum convective heating at 40.7-km altitude and 6592-m/s velocity. The density and temperature of the CO_2–N_2 gas at this altitude are 3.24×10^{-4} kg/m^3 and 162 K. This trajectory point is examined first and referred to as the maximum-heating point. The maximum-deceleration or maximum-pressure point examined occurs at 28.5-km altitude at a speed of 4862 m/s. The atmospheric density and temperature are 1.161×10^{-3} kg/m^3 and 176.8 K at this altitude. Flight Reynolds numbers based on vehicle diameter for these two trajectory points are 0.64×10^6 and 1.53×10^6, respectively.

Maximum-Heating-Point Results

The forebody pressure prediction from a nonablating solution at the maximum heating point is compared with that predicted by a viscous shock layer (VSL) method[23] in Fig. 1. Both solutions display blunted cone distributions. The variable s is the distance along the surface from the stagnation point. An s value of 1.437 m corresponds to the vehicle's shoulder. Differences in the shoulder region might originate from differences in the two methods or from the VSL method's forebody-only computation.

The forebody convective heating predictions (nonablating) are compared in Fig. 2. The stagnation-point value from the present method is 115 W/cm^2, whereas the VSL method predicts a value of 126.5 W/cm^2. Both solutions predict a stagnation-point value for the CO_2 mass fraction of 0.83. In addition to different governing equations and solution techniques, the two methods use different diffusion models.

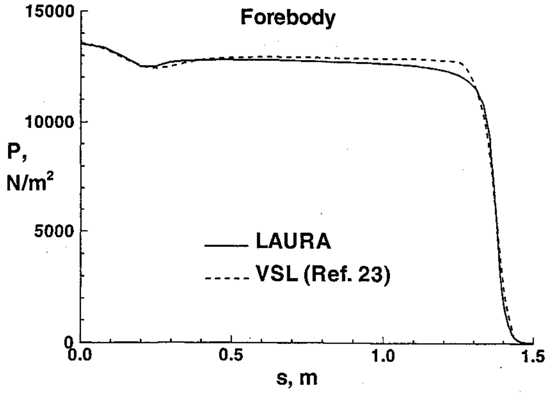

Fig. 1 Comparison of pressure distributions on the forebody surface (V = 6592 m/s, alt. = 40.7 km).

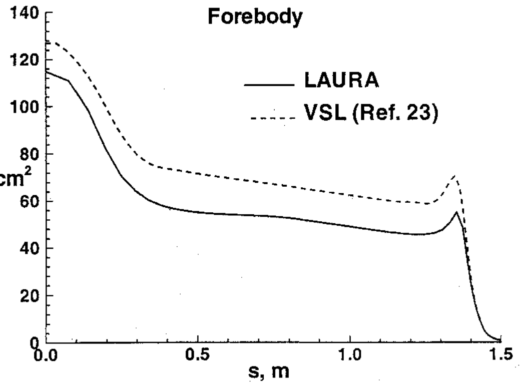

Fig. 2 Comparison of convective-heating distributions on the nonablating forebody surface (V = 6592 m/s, alt. = 40.7 km).

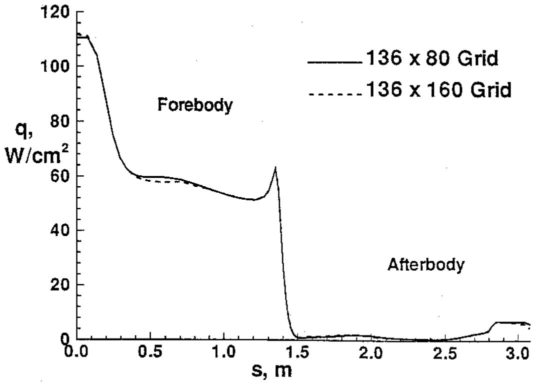

Fig. 4 Comparison of heating predictions on forebody and afterbody from grid resolution study in Ref. 15 (nonablating, V = 6500 m/s, alt. = 40.5 km).

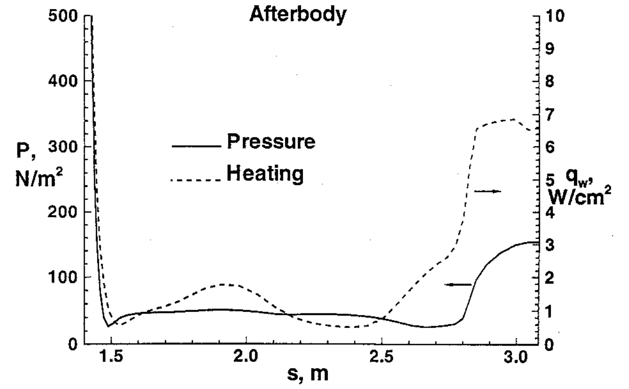

Fig. 3 Pressure and convective-heating distributions on the afterbody surface (V = 6592 m/s, alt. = 40.7 km).

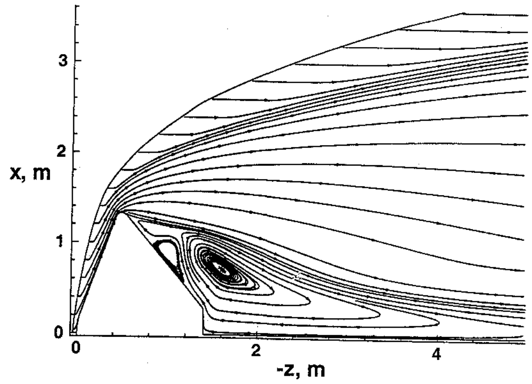

Fig. 5 Close-up of streamlines in near-wake region (nonablating, V = 6592 m/s, alt. = 40.7 km).

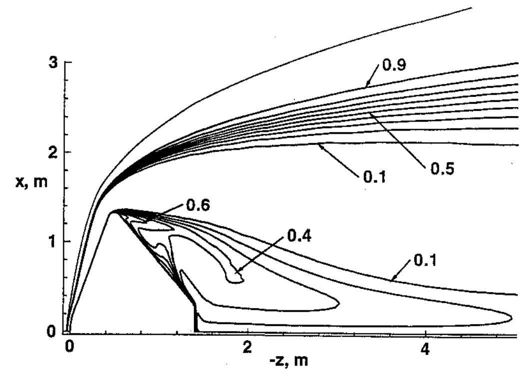

Fig. 6 Contours of CO_2 mass fraction (nonablating, V = 6592 m/s, alt. = 40.7 km).

Numerous approximate methods exist to estimate the stagnation heating on entry vehicles. The cold-wall correlation due to Sutton and Graves[24] for the Mars atmosphere is

$$q_w = 1.89 \times 10^{-08} R_{N,\mathrm{eff}}^{-0.5} \rho_\infty^{0.5} V_\infty^3 \tag{29}$$

where $R_{N,\mathrm{eff}}$ is the effective nose radius in meters and q_w is in W/cm². When the actual nose radius of 0.6625 m is used, the correlation predicts a value of 119.7 W/cm² for this case.

On the afterbody (Fig. 3), the highest pressure and convective heating occur on the flat stern. An s value of 2.83 m corresponds to the corner between the afterbody cone and flat stern of the vehicle. The maximum base pressure is 154 N/m², or 1.1% of the stagnation pressure. The maximum base heating is 6.7 W/cm², or 5.9% of the stagnation value. The vehicle's drag coefficient is predicted to be 1.69.

Flight data from the two Viking missions[25,26] indicate that the base pressure is approximately 1% of the stagnation-point pressure for similar points in its trajectory. Preflight Viking predictions anticipated a base heating rate equal to 2% of the stagnation-point value. Reference 25 states the flight data exceeded that prediction and reports a value of 4.2% for apparent base heating. The Viking probes, however, entered at 11-deg angle of attack and speeds near 3500 m/s. In addition, the locations of the pressure transducers and thermocouples were not necessarily the locations of maximum pressure and heating.

A grid resolution study was performed in Ref. 15. The freestream velocity of 6500 m/s and density of 3.19×10^{-4} kg/m³ for that study are similar to the maximum-heating conditions examined here. Figure 4 (from Ref. 15) compares the convective heating prediction from a 136 × 80 grid like the one used in the present study with a 136 × 160 grid. Based on this comparison, the 136 × 80 grid is judged as adequate.

In the present axisymmetric solution, the maximum afterbody base pressure and heating are the result of impingement by a strong recirculation vortex. A close-up of this vortex is shown in Fig. 5. The vortex extends downstream to a free-shear-layer stagnation point 5.17 m from the nose. A weak secondary vortex exists just behind the shoulder and is also indicated in Fig. 3. (The three-dimensional manifestations of these axisymmetric vortices are toroidal in shape.)

The flow in the nose and conical regions of the forebody is subsonic. The subsonic-zone deflection angle around the vehicle's shoulder is 11 deg.

A question arises as to the chemical state of the near wake. Rapid expansion of reacting flows can result in chemically frozen flow. Figure 6 presents contours of CO_2 mass fraction for the near-wake flowfield. The figure indicates the source of CO_2 in the wake results from the boundary condition, which forces CO_2 recombination. The CO_2 so recombined on the forebody and afterbody is then entrained in the recirculation vortex.

The radiative heating expected for the maximum-heating case is estimated by several methods. The equilibrium method of Ref. 27 predicts a value of 5.5 W/cm² at the stagnation-point. A more detailed forebody calculation using the LORAN code of Hartung[28] predicts stagnation-point radiative heating at 12.5 W/cm^2. The equilibrium VSL method of Ref. 23 predicts 5.7 W/cm^2.

Ablating Solution

The mass blowing rate and surface temperature from the coupled material-response analysis for this trajectory point are presented in Fig. 7. The nearly constant blowing rate is about 1% of the freestream mass flux. The mass fractions of the blown species existing on the solid side of the wall interface are shown in Fig. 8. A full vehicle solution is generated using these quantities on the forebody and nonablating, radiative-equilibrium wall-temperature boundary conditions on the afterbody.

The effect of ablation on the pressure distribution is negligible; its effect on forebody heating is shown in Fig. 9. Ablation injection decreases convective heating at the stagnation point by 18%. The equilibrium VSL analysis of Ref. 23 reports a 9% reduction in stagnation point heating due to ablation for this case. On the afterbody, convective heating remains unchanged. Mass-fraction contours of the ablation product SiO are shown in Fig. 10. Concentrations as high as 0.2 exist just behind the shoulder. The SiO molecules are captured in the recirculation vortex and then diffuse. Including ablation causes little change in the near-wake streamlines, and the resulting recirculation zone is like that shown in Fig. 5. Lower wall recombination rates for CO_2 due to the presence of ablation products, however, result in lower recirculation-zone concentrations of that species than those shown in Fig. 6.

Maximum-Deceleration-Point Results

Nonablating results for the Mach 22, maximum-pressure trajectory point are discussed next. Predictions of the forebody pressure and convective heating are presented in Fig. 11. Figure 12 presents the afterbody heating and pressure. For this trajectory point, the base pressure is 1.4% of its 26,525-N/m^2 stagnation value. The afterbody heating is 7.0 W/cm^2, a value equal to that predicted at the maximum heating point. The maximum afterbody heating is then 10% of the stagnation-point value. The near-wake flow structure is similar

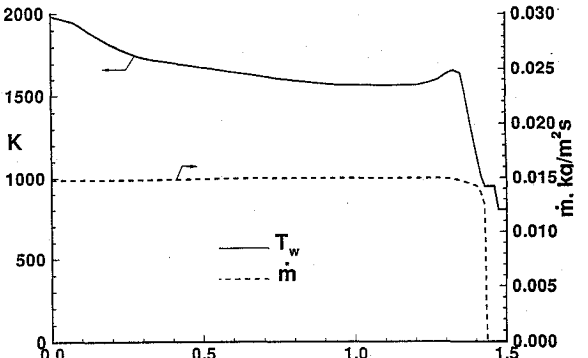

Fig. 7 Blowing rate and wall temperature from ablation analysis (V = 6592 m/s, alt. = 40.7 km).

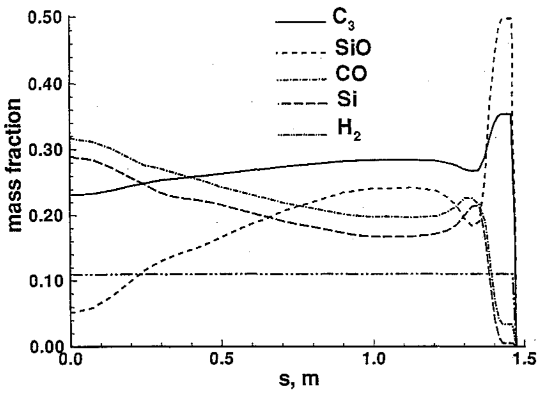

Fig. 8 Species composition of ablation injection (V = 6592 m/s, alt. = 40.7 km).

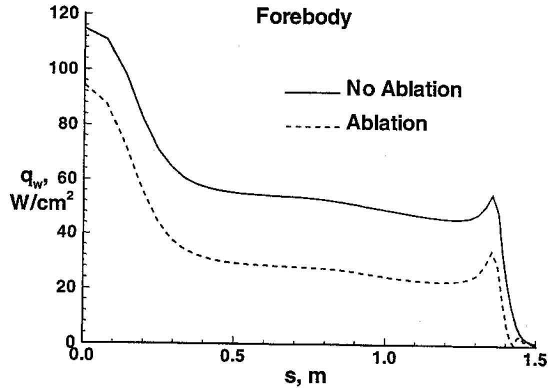

Fig. 9 Effect of ablation on forebody heating (V = 6592 m/s, alt. = 40.7 km).

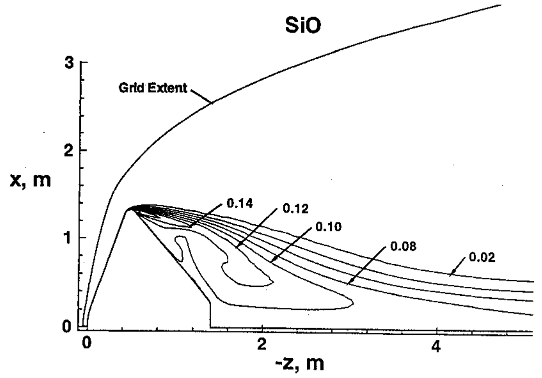

Fig. 10 Contours of mass fraction of SiO in ablating case (V = 6592 m/s, alt. = 40.7 km).

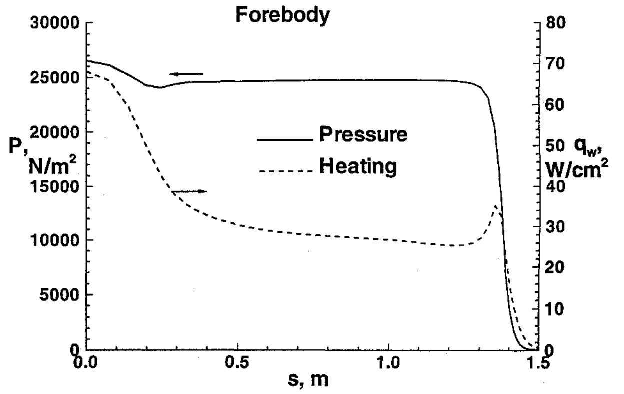

Fig. 11 Forebody pressure and convective heating at maximum deceleration point in trajectory (nonablating, V =4862 m/s, alt. = 28.5 km).

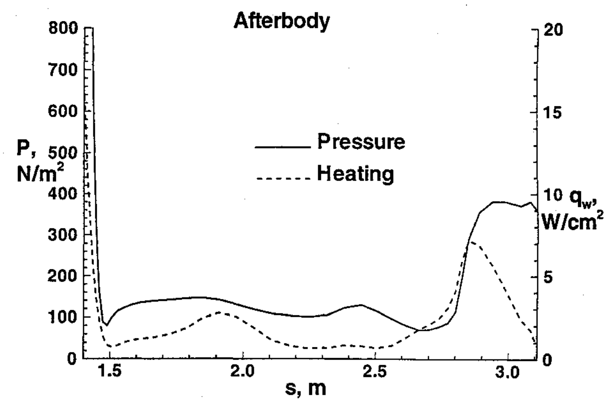

Fig. 12 Afterbody pressure and convective heating at maximum deceleration point in trajectory (nonablating, V = 4862 m/s, alt. = 28.5 km).

to that shown in Figs. 5 and 6, except the primary recirculation vortex is smaller, with the free-shear-layer stagnation point at 4.41 m downstream of the nose. The drag coefficient for this case is predicted to be 1.71. The stagnation-point radiative-heating estimate for this case is less than 0.1 W/cm^2.

Conclusions

The convective heating at the stagnation point computed for the nonablating maximum-heating trajectory point is 115 W/cm^2. The maximum afterbody heating and pressure for this zero-angle-of-attack case occur on the vehicle's stern. These maxima result from the focused impingement of a large recirculation vortex, and the maximum afterbody pressure is near 1% of the stagnation pressure. The maximum afterbody convective heating is 5.9% of the stagnation value. These ratios are consistent with Viking flight data. Radiative heating on the forebody is 5–11% of the convective heating.

The effect of forebody ablation with blowing rate at 1% of freestream mass flux is to decrease the forebody convective heating 18% at the stagnation-point. The decrease on the forebody flank is as high as 50%. Products from the forebody ablation become entrained in the recirculation vortex, but they have little effect on wake structure and afterbody surface pressure and heating.

Nonablating results from the maximum deceleration point in the trajectory estimate the maximum stagnation-point pressure at 26,525 N/m^2. While forebody convective heating levels are 40–50% lower than those predicted at the maximum-heating trajectory point, the afterbody convective-heating values are nearly equal.

Acknowledgments

Sincere thanks are extended to Stephen Alter for generating the computational grids for this study. Thanks are also extended to W. Henline, Y.-K. Chen, and D. Olynick of the NASA Ames Research Center for many helpful discussions. R. Gupta was instrumental in establishing the boundary conditions. W. Henline and Y.-K. Chen supplied the ablation injection quantities. Lin Hartung Chambers supplied the radiative-heating estimates.

References

[1] Hubbard, G. S., Wercinski, P. F., Sarver, G. L., Hanel, R. P., and Ramos, R., "A Mars Environmental Survey (MESUR)—Feasibility of a Low Cost Global Approach," International Astronautical Federation, Paper 91-432, Oct. 1991.

[2] Bourke, R. D., Golombek, M. P., Spear, A. J., and Sturms, F. M., "MESUR and Its Role in an Evolutionary Mars Exploration Program," International Astronautical Federation, Paper 92-0509, Sept. 1992.

[3] Mitcheltree, R. A., "Aerothermodynamics of a MESUR Martian Entry," AIAA Paper 93-2761, July 1993.

[4] Chen, Y.-K., Henline, W. D., Stewart, D. A., and Candler, G. V., "Navier–Stokes Solutions with Surface Catalysis for Martian Atmospheric Entry," *Journal of Spacecraft and Rockets*, Vol. 30, No. 1, 1993, pp. 32–42.

[5] Tauber, M., Henline, W., Chargin, M., Papadopoulos, P., Chen, Y.-K., Yang, L., and Hamm, K., "MESUR Probe Aerobrake Preliminary Design Study," *Journal of Spacecraft and Rockets*, Vol. 30, No. 4, 1993, pp. 431–437.

[6] Papadopoulos, P., Tauber, M., and Chang, I.-D., "Aerobraking in a Dusty Martian Atmosphere," AIAA Paper 90-1700, June 1990.

[7] Park, C., Howe, J. T., Jaffe, R. L., and Candler, G. V., "Chemical Kinetic Problems of Future NASA Missions," AIAA Paper 91-0464, Jan. 1991.

[8] Candler, G. V., "Computation of Thermo-Chemical Nonequilibrium Martian Atmosphere Entry Flows," AIAA Paper 90-1695, June 1990.

[9] Gupta, R. N., Lee, K. P., Moss, J. N., and Sutton, K., "A Viscous-Shock-Layer Analysis of the Martian Aerothermal Environment," AIAA Paper 91-1345, June 1991.

[10] Kay, R. D., and Netterfield, M. P., " Thermochemical Non-Equilibrium Computations for a Mars Entry Vehicle," AIAA Paper 93-2841, July 1993.

[11] Gnoffo, P. A., Gupta, R. N., and Shinn, J. L., "Conservation Equations and Physical Models for Hypersonic Air Flows in Thermal and Chemical Nonequilibrium," NASA TP-2867, Feb. 1989.

[12] Gnoffo, P. A., "An Upwind-Biased, Point-Implicit Relaxation Algorithm for Viscous, Compressible Perfect-Gas Flows," NASA TP-2953, Feb. 1990.

[13] Gnoffo, P. A., "Computation of Near-Wake, Aerobrake Flowfields," *Journal of Spacecraft and Rockets*, Vol. 29, No. 2, 1992, pp. 182–189.

[14] Gnoffo, P. A., Weilmuenster, K. J., and Alter, S. J., "A Multiblock Analysis for Shuttle Orbiter Re-Entry Heating from Mach 24 to Mach 12," AIAA Paper 93-2813, July 1993.

[15] Mitcheltree, R. A., and Gnoffo, P. A., "Wake Flow About a MESUR Mars Entry Vehicle," AIAA Paper 94-1958, June 1994.

[16] Willey, R. J., "Comparison of Kinetic Models for Atom Recombination on High-Temperature Reusable Surface Insulation," *Journal of Thermophysics and Heat Transfer*, Vol. 7, No. 1, 1993.

[17] Lee, J.-H., "Basic Governing Equations for the Flight Regimes of Aeroassisted Orbital Transfer Vehicles," *Thermal Design of Aeroassisted Orbital Transfer Vehicles*, edited by H. F. Nelson, Vol. 96, Progress in Astronautics and Aeronautics, AIAA, New York, 1985, pp. 3–53.

[18] Chen, Y.-K., Henline, W. D., and Tauber, M. E., "Mars Pathfinder Trajectory Based Heating and Ablation Calculations," *Journal of Spacecraft and Rockets*, Vol. 32, No. 2, 1995, pp. 225–230.

[19] Bartlett, E. P., and Kendall, R. M., "Aerotherm Charring Material Thermal Response and Ablation Program (CMA87S)," Acurex, Rept. UM-87-13/ATD, Nov. 1987.

[20] Steger, J. L., and Rizk, Y. M., "Generation of Three-Dimensional Body-Fitted Coordinates Using Hyperbolic Partial Differential Equations," NASA TM-86753, 1985.

[21] Steinbrenner, J. P., Chawner, J. R., and Fouts, C. L., "The GRIDGEN 3D Multiple Block Grid Generation System," Wright Research and Development Center, Rept. WRDC-TR-90-3022, Oct. 1989.

[22] Alter, S. J., and Weilmuenster, K. J., "The Three-Dimensional Multi-Block Advanced Grid Generation System (3DMAGGS)," NASA TM-108985, April 1993.

[23] Gupta, R. N., "An Aerothermal Study of the MESUR Pathfinder Aeroshell," AIAA Paper 94-2025, June 1994.

[24] Sutton, K., and Graves, R. A., "A General Stagnation-Point Convective-Heating Equation for Arbitrary Gas Mixtures," NASA TR-102659, May 1990.

[25] Inogoldby, R. N., Michel, F. C., Flaherty, T. M., Doty, M. G., Preston, B., Villyyard, K. W., and Steele, R. D., "Entry Data Analysis for Viking Landers 1 and 2," NASA CR-159388, Nov. 1976.

[26] Schmitt, D. A., "Base Heating on an Aerobraking Orbital Transfer Vehicle," AIAA Paper 83-0408, Jan. 1983.

[27] Hartung, L. C., Sutton, K., and Brauns, F., "Equilibrium Radiative Heating Tables for Aerobraking in the Martian Atmosphere," NASA TM-102659, May 1990.

[28] Hartung, L. C., "Development of a Nonequilibrium Radiative Heating Prediction Method for Coupled Flowfield Solutions," *Journal of Thermophysics and Heat Transfer*, Vol. 6, No. 4, 1992, pp. 618–625.

T. C. Lin
Associate Editor